Quantifying the vertical transport of $CHBr_3$ and CH_2Br_2 over the Western Pacific

Robyn Butler[1], Paul I. Palmer[1], Liang Feng[1], Stephen J. Andrews[2], Elliot L. Atlas[3], Lucy J. Carpenter[2], Valeria Donets[3], Neil R. P. Harris[4], Stephen A. Montzka[5], Laura L. Pan[6], Ross J. Salawitch[7], and Sue M. Schauffler[6]

[1]School of GeoSciences, University of Edinburgh, UK
[2]Department of Chemistry, Wolfson Atmospheric Chemistry Laboratories, University of York, UK
[3]University of Miami, Florida, USA
[4]Department of Chemistry, University of Cambridge, UK
[5]National Oceanic and Atmospheric Administration, Boulder, USA
[6]National Center for Atmospheric Research, Boulder, Colorado, USA
[7]University of Maryland, College Park, Maryland, USA

Correspondence to: R. Butler (r.butler-2@sms.ed.ac.uk)

Abstract. We use the GEOS-Chem global 3-D atmospheric chemistry transport model to interpret atmospheric observations of bromoform ($CHBr_3$) and dibromomethane (CH_2Br_2) collected during the CAST and CONTRAST aircraft measurement campaigns over the Western Pacific, January–February, 2014. We use a new linearised, tagged version of $CHBr_3$ and CH_2Br_2, allowing us to study the influence of emissions from specific geographical regions on observed atmospheric variations. The model describes 32%–37% of $CHBr_3$ and 15%-45% of CH_2Br_2 observed variability during CAST and CONTRAST, reflecting model errors in vertical transport. The model has a mean positive bias of 30% that is larger near the surface reflecting errors in the poorly constrained prior emission estimates. We find using the model that observed variability of $CHBr_3$ and CH_2Br_2 is driven by open ocean emissions where there is deep convection. Atmospheric variability above >6km includes a significant contribution from coastal oceans, but it is still dominated by emissions from the open ocean and by older air masses that originate upwind. In the absence of reliable ocean emission estimates, we use a new physical age of air simulation to determine the relative abundance of halogens delivered by $CHBr_3$ and CH_2Br_2 to the tropical transition layer (TTL). We find that 76% (92%) of air masses that originate from the ocean reach the TTL within two (three) atmospheric e-folding lifetimes of $CHBr_3$ and almost all of them reach the TTL within one e-folding lifetime of CH_2Br_2. Over the duration of CAST and CONTRAST, and over our study region, oceans delivered a mean (range) $CHBr_3$ and CH_2Br_2 mole fraction of 0.46 (0.13–0.72) and 0.88 (0.71–1.01) pptv, respectively, to the TTL, and a mean (range) Br_y mole fraction of 3.14 (1.81–4.18) pptv from source gases to the upper troposphere.

1 Introduction

Halogenated very short-lived substances (VSLS) are gases that have a tropospheric e-folding lifetime of <6 months. This lifetime is shorter than the characteristic timescale associated with atmospheric transport of material from the surface to the

tropopause. Natural sources of VSLS represent a progressively larger fraction of the inorganic halogen budget in the strato-sphere that drives halogen-catalysed ozone loss, as anthropogenic halogenated compounds continue to decline in accordance with international agreements. Quantifying the magnitude and variation of these natural VSLS fluxes to the stratosphere is therefore a research priority for environmental science. VSLS include a wide range of gases such as bromoform ($CHBr_3$), di-

5 bromomethane (CH_2Br_2), bromochloromethane (CH_2BrCl), dibromochloromethane ($CHBr_2Cl$), and bromodichloromethane ($CHBrCl_2$). Here we focus on $CHBr_3$ and CH_2Br_2, which collectively represent >80% of the organic bromine in the marine boundary layer and upper troposphere, and are dominated by marine sources (WMO, 2007). We use aircraft observations of $CHBr_3$ and CH_2Br_2 collected over the western Pacific in January and February 2014 to quantify the regional flux of these compounds to the stratosphere.

10 The main sources of $CHBr_3$ and CH_2Br_2 include phytoplankton, particularly diatoms, and various species of seaweed (Carpenter and Liss, 2000; Quack and Wallace, 2003; Carpenter et al., 2014). The magnitude and distribution of these emissions reflect supersaturation of the compounds and nutrient-rich upwelling waters (Quack et al., 2007). Tropical, subtropical and shelf waters are important sources of $CHBr_3$ and CH_2Br_2 with high spatial and temporal variability (Ziska et al., 2013). Current emission inventories, informed by sparse ship-borne data, have large uncertainties (Warwick et al., 2006; Liang et al., 2010;

15 Ordóñez et al., 2012; Tegtmeier et al., 2012; Hossaini et al., 2013; Ziska et al., 2013). The atmospheric lifetime of $CHBr_3$ is ~24 days, determined primarily by photolysis and to a lesser extent by OH oxidation. CH_2Br_2 has an atmospheric lifetime of ~123 days determined by OH oxidation (Ko and Poulet, 2003).

Vertical ascent of $CHBr_3$ and CH_2Br_2 and their oxidation products to the upper troposphere lower stratosphere (UTLS) represent a source of bromine that acts as a catalyst for ozone loss in the stratosphere. Balloon-borne and satellite observations

20 estimate that brominated VSLS and their degradation products contribute 2–8 ppt to stratospheric Br_y (Sinnhuber et al., 2002, 2005; Sioris et al., 2006; Dorf et al., 2008; McLinden et al., 2010; Salawitch et al., 2010). Model estimates range between 2 and 7 ppt for this contribution (Aschmann et al., 2009; Hossaini et al., 2010; Liang et al., 2010; Ordóñez et al., 2012; Fernandez et al., 2014). This contribution mainly originates from areas of deep convection over the tropical Indian ocean, Western Pacific, and off the Pacific coast of Mexico (Gettelman et al., 2002; Fueglistaler et al., 2004; Aschmann et al., 2009;

25 Ashfold et al., 2012; Hossaini et al., 2012). The stratospheric community has categorized two methods of delivering VSLS to the stratosphere: 1) source gas injection (SGI), which describes the direct transport of the emitted halogenated compounds (e.g., $CHBr_3$ and CH_2Br_2); and 2) product gas injection (PGI), which refers to the transport of the degradation products of these emitted compounds. Previous model-based calculations (Hossaini et al., 2012; Tegtmeier et al., 2012; Aschmann and Sinnhuber, 2013; Liang et al., 2014) have estimated that 15%-75% of the stratospheric inorganic bromine budget from VSLS

30 is delivered by SGI, with uncertainty of the total Br_y reflecting uncertainty of wet deposition of PGI product gases in the UTLS (Sinnhuber and Folkins, 2006; Liang et al., 2014).

The tropical tropopause layer (TTL) represents a gradual transition from the troposphere to the stratosphere (Zhou et al., 2004; Fueglistaler et al., 2009; Pan et al., 2014). It extends over a few kilometres within the upper troposphere between where the atmospheric lapse rate is at a minimum (~12–13 km) and the cold point tropopause (~17 km) (Gettelman and Forster,

35 2002). The TTL is the dominant transport pathway for SGI and PGI gases to the lower stratosphere. TTL temperatures vary

zonally with the smallest values between $130°-180°E$ throughout the year, corresponding to the tropical warm pool over the Western Pacific where convective activity is largest (Gettelman et al., 2002). Estimates of SGI within this region are highly dependent on the strength and spatial variability of source regions, and how they couple with atmospheric transport mechanisms.

5   We use data from two coordinated aircraft campaigns over the western Pacific during 2014, the Co-ordinated Airborne Studies in the Tropics (CAST, Harris et al. (2016)) and the CONvective Transport of Active Species in the Tropics (CONTRAST, Pan et al. (2016)), to study the emission, vertical transport, and chemical transformation of halogenated gases. The CAST and CONTRAST campaigns measured a suite of trace gases and aerosols centred on the Micronesian region in the western Pacific, including Guam, Chuuk, and Palau during January and February 2014. We interpret aircraft measurements of $CHBr_3$

10   and CH_2Br_2 mole fraction using the GEOS-Chem atmospheric chemistry transport model.

In the next section we describe CAST and CONTRAST and the data we used. Section 3 describes the GEOS-Chem model and how it is used to interpret the airborne data. In section 4 we evaluate the model and describe our results. We conclude the paper in section 5.

2   Observational data

15   **2.1   CAST and CONTRAST $CHBr_3$ and CH_2Br_2 mole fraction data**

We use $CHBr_3$ and CH_2Br_2 mole fractions from the CAST and CONTRAST aircraft campaigns (Harris et al., 2016; Pan et al., 2016). Here for the sake of brevity we provide only brief details about the $CHBr_3$ and CH_2Br_2 data and refer the reader to Andrews et al. (2016) for a more comprehensive description of the data collection and analysis procedures used during the campaigns.

20   Figure 1 shows the spatial distribution of whole air samples (WAS) collected during CAST and CONTRAST. For CAST, WAS canisters were filled aboard the Facility for Airborne Atmospheric Measurements (FAAM) BAe-146 aircraft. These canisters were analysed for $CHBr_3$ and CH_2Br_2 and other trace compounds within 72 hours of collection. The WAS instrument was calibrated using the National Oceanic and Atmospheric Administration (NOAA) 2003 scale for $CHBr_3$ and the NOAA 2004 scale for CH_2Br_2. For CONTRAST, a similar WAS system was employed to collect $CHBr_3$ and CH_2Br_2 measurements

25   on the NSF/NCAR Gulfstream-V HIAPER (High-performance Instrumented Airborne Platform for Environmental Research) aircraft. A working standard was used to regularly calibrate the samples, and that working standard was calibrated using a series of dilutions of high concentration standards that are linked to National Institute of Standards and Technology standards. The mean absolute percentage error for $CHBr_3$ and CH_2Br_2 measurements between $0-8$ km is 7.7% and 2.2%, respectively, representing the combined error between the two WAS systems and two accompanying GC/MS instruments.

30   Table 1 shows mean measurement statistics of $CHBr_3$ and CH_2Br_2 for the CAST and CONTRAST campaigns. $CHBr_3$ is generally more variable than CH_2Br_2 throughout the study region, reflecting its shorter atmospheric lifetime, so that sampling differences between CAST and CONTRAST will introduce larger differences for this gas. CAST measurements of $CHBr_3$ are typically lower than for CONTRAST, but CAST recorded the highest and lowest $CHBr_3$ mole fractions at $0-2$ km and

6−8 km, respectively. We define the TTL from 13 km (Pan et al., 2014) to the local tropopause determined from the GEOS5–FP analysed meteorological fields, as described below. CONTRAST measured a minimum $CHBr_3$ value indistinguishable from zero just below the TTL at 10–13 km. Measurements of CH_2Br_2 are generally consistent between CAST and CONTRAST at all altitudes. There is only a small vertical gradient for CH_2Br_2 above 2 km with a mean value of $\sim$0.91 pptv. CONTRAST measured the lowest value of 0.21 pptv just below the TTL. Within the TTL, CONTRAST reports mean (maximum) values of 0.42 pptv (0.85 pptv) and 0.84 pptv (1.05 pptv) for $CHBr_3$ and CH_2Br_2, respectively, providing some evidence of rapid convection of surface emissions to the upper troposphere.

2.2 NOAA ground-based $CHBr_3$ and CH_2Br_2 measurements

Table 2 summarises the independent surface measurements of $CHBr_3$ and CH_2Br_2 collected by the NOAA Earth System Research Laboratory (ERSL) we have used to evaluate the GEOS-Chem atmospheric chemistry model simulation on a global scale. This evaluation was undertaken to report on model performance and is not used to provide additional data over the Western Pacific.

These measurements are part of the ongoing NOAA/ESRL global monitoring program (http://www.esrl.noaa.gov/gmd). $CHBr_3$ and CH_2Br_2 measurements are obtained approximately weekly using paired steel flasks, which are then analysed by GC/MS. Further details about their sampling are given in Montzka et al. (2011). In Appendix A, we evaluate the model using mean monthly statistics at each sites from 1st January 2005 to 31 December 2011.

3 The GEOS-Chem Global 3-D Atmospheric Chemistry Transport Model

To interpret CAST and CONTRAST data we use v9.02 of the GEOS-Chem global 3-D atmospheric chemistry transport model (www.geos-chem.org), driven by GEOS5–FP analysed meteorological fields provided by the Global Modelling and Assimilation Office (GMAO) at NASA Goddard Space Flight Centre. For our experiments we degrade the native meteorological fields to a model horizontal spatial resolution of $2°$ latitude $\times$ $2.5°$ longitude described on 47 vertical levels, with a top pressure of 0.01 hPa. Dynamic tropopause height and convective mass flux (CMF) from the meteorological fields are given on a 1–hourly and 3–hourly averaging period, respectively.

We describe below two new GEOS-Chem simulations that we developed to interpret observed variations of $CHBr_3$ and CH_2Br_2 during CAST and CONTRAST airborne campaigns: 1) a tagged simulation of $CHBr_3$ and CH_2Br_2 to better understand source attribution; and 2) an age of air simulation to improve understanding of the vertical transport of these short-lived halogenated compounds. For both simulations, we sample the model at the time and location of CAST and CONTRAST observations.

3.1 Tagged $CHBr_3$ and CH_2Br_2 Simulation

The purpose of this simulation is to relate observed atmospheric variations to surface emissions from individual sources and/or geographical regions. To achieve this we use pre-computed monthly 3-D fields of OH and photolysis rates for $CHBr_3$ and

CH_2Br_2 from the full-chemistry version of GEOS-Chem, allowing us to linearise the chemistry so that we can isolate the contributions from individual sources and geographical regions.

The structure of the model framework follows closely other tagged simulations within GEOS-Chem (e.g., Jones et al. (2003); Palmer et al. (2003); Finch et al. (2014); Mackie et al. (2016)). We use the following temperature (T) dependent

5   reaction rate constants that describe oxidation of $CHBr_3$ and CH_2Br_2 by OH (Sander et al., 2011): for $CHBr_3$, $k(T) = 1.35 \times 10^{-12} \exp(-600/T)$ cm^{3}molec^{-1}s^{-1}; and for CH_2Br_2, $k(T) = 2.00 \times 10^{-12} \exp(-840/T)$ cm^{3}molec^{-1}s^{-1}.

Figure 2 shows the magnitude and spatial distribution of our prior emissions of $CHBr_3$ and CH_2Br_2 (Liang et al., 2010). These emission estimates were derived from airborne measurements in the troposphere and lower stratosphere over the Western Pacific and North America. Liang et al. (2010) has global annual totals of 425 Gg Br yr^{-1} for $CHBr_3$ and 57 Gg Br yr^{-1}

10 for CH_2Br_2. These emissions integrated over the geographical region and duration of the campaign are 3 Gg Br yr^{-1} and 0.4 Gg Br yr^{-1} for $CHBr_3$ and CH_2Br_2, respectively. We temporally distribute emissions every 30 minutes without any diurnal variation. We found that other commonly-used emission inventories for $CHBr_3$ and CH_2Br_2 (e.g. Ordóñez et al. (2012) and Ziska et al. (2013)) were not noticeably better than Liang et al. (2010) at describing the CAST and CONTRAST data (not shown). We chose to use Liang et al. (2010) because it has a consistent bias for $CHBr_3$ and CH_2Br_2.

15 Figure 3 shows the ocean (open and coastal) tagged tracer regions we use in the GEOS-Chem model. These geographical definitions are informed by the NOAA ETOPO2v2 Global Relief map (National Geographic Data Center, NOAA, 2006), which combines topography and ocean depth data at 2 minute spatial resolution: heights between 0 and -200 m are defined as coastal oceans; and heights below -200 m are open ocean. Each 2 minute cell that falls within a model grid box is assigned a coastal or open ocean. Each model grid box can then be described as fractional contributions (R_x) to the open and coastal ocean tagged

20 regions. We have explicitly included elevated coastal emissions from the inventory in to the coastal tracer. We assign individual tracers to major islands within our study domain, including Guam (13.5°N, 144.8°E), Chuuk (7.5°N, 151.8°E), Palau (7.4°N, 134.5 °E), and Manus (2.1 °S, 147.4 °E). We assume these island land masses account for 100% of a grid box irrespective of whether their area fills the grid box. This gives a total of 18 tagged tracers, evenly split between $CHBr_3$ and CH_2Br_2 including a total tracer and a background tracer.

25 For global model evaluation using the NOAA data, described above, we initialize model tagged tracers in January 2004 with near-zero values and run the simulation to January 2013. We discard the first model year to minimize the impact of the initial conditions. For model evaluation using the CAST/CONTRAST data, we initialize the tagged tracers in January 2014 with near-zero values. Background initial conditions were determined from a 12-month integration of the full-chemistry model, which are then in the tagged model subject to atmospheric transport and loss processes. For model evaluation, we sample at

30 the time and location of each observation. For the NOAA data described above, we calculate monthly mean statistics from 1st January 2005–31 December 2011.

3.2 Physical age of air model calculation

We use the age of air simulation to understand how short-lived halogenated compounds are transported to the TTL, independent of emission inventories. The method uses only knowledge of the distribution of emissions, and not the magnitude, so we

investigate the influence of emissions source region with respect to respective CHBr$_3$ and CH$_2$Br$_2$ atmospheric e-folding lifetimes. We use the GEOS-Chem model to determine the physical age of air A, building on previous studies (Finch et al., 2014), and use a consistent set of geographical regions used in our tagged CHBr$_3$ and CH$_2$Br$_2$ simulations (Figure 3).

For each model tracer we define a surface boundary volume mixing ratio B that linearly increases with time t so that smaller values correspond to older physical ages:

$$B = f \times t, \tag{1}$$

where f is a constant (1×10^{-15} s^{-1}). B describes a volume mixing ratio of each tracer dependent on their time of emission. Fractional contributions of tracers are calculated based on R_x where the finalised B (B_{final}) in the surface boundary condition is calculated using:

$$B_{final} = (B \times R_x) + (1 - R_x \times X) \tag{2}$$

where X denotes the mixing ratio of tracer within the grid box. As time progresses, smaller volume mixing ratios represent older ages that have spent more time away from the surface boundary.

We initialise this model in July 2013 and run for six months until the start of January 2014 so that at least one e-folding lifetime of CH$_2$Br$_2$ has been achieved. We then sample the resulting 3-D field of model tracer mixing ratios (X), at the time and location of CAST and CONTRAST measurements. The physical age of a tracer A since it last came into contact with an ocean surface is given by:

$$A = t - X/f \tag{3}$$

We account for atmospheric dispersion by using the GEOS-Chem model, but we do not consider any chemical losses.

To explicitly evaluate marine convection in GEOS-Chem we also developed a short-lived tagged tracer simulation with an e-folding lifetime of four days, comparable to that of methyl iodide (CH$_3$I) in the tropics (Carpenter et al., 2014). We emit the tracer with an equilibrium mole fraction of 1 pptv over all oceanic regions described in Figure 3. We initialise the model on 1st January 2014 with an empty 3-D atmospheric field and run for two months until 01/03/2014. Model output is archived every two hours and the model is sampled along the aircraft flight tracks. By comparison our model with CH$_3$I observations, we find that GEOS-Chem captures mean marine convective flow over the study region. We also find that the model captures fast, infrequent large-scale convective transport that result in upper tropospheric ages of 3–5 days, but does not capture small-scale variations due to rapid convection. Appendix B includes a more detailed report on the results.

4 Results

4.1 Model Evaluation

We evaluate our tagged model of atmospheric CHBr$_3$ and CH$_2$Br$_2$ using NOAA surface data, and CAST and CONTRAST aircraft data during January and February 2014.

Model evaluation using the NOAA data is described in Appendix A. In brief, the model generally has a positive bias but reproduces 30–60% of the seasonal variation (Pearson correlation coefficients in Table 3), depending on geographical location. Model errors in reproducing the observed seasonal cycle reflect errors in production and loss rates. The model generally has less skill at reproducing observations collected at coastal sites close to emission sources.

Figure 4 shows that CAST and CONTRAST observed and model vertical profiles $CHBr_3$ and CH_2Br_2 have an inverted 'S' shape (Harris et al., 2016; Pan et al., 2016). The suggests that GEOS-Chem has skill in describing the the broad-scale atmospheric transport over the study region. From Pearson correlation coefficients, we find that GEOS-Chem reproduces more than 30% of the observed variability of $CHBr_3$ from CAST and CONTRAST and between 15% (CAST) and 45% (CONTRAST) of the observed variability of CH_2Br_2. Larger differences in the correlations for CH_2Br_2 is likely due to differences in the the sampled air masses that have originated far upwind. Figure 4 also shows that GEOS-Chem has a positive model bias of 30% for both campaigns, which we calculate using: $100/N_i\Sigma_i(mod_i - obs_i)/(max(mod_i, obs_i))$. The relative model error is reasonably constant with altitude for $CHBr_3$ and CH_2Br_2, suggesting that this bias is representative of prior surface emissions. Consequently, we remove this bias from subsequent calculations. We attribute the variations about the mean bias to errors due to model atmospheric transport.

4.2 Tagged-VSLS Model Output

Figure 5 and Figure 6 show a strong region of convection south of Chuuk and along the equator that transports $CHBr_3$ and CH_2Br_2 directly from open oceanic emission sources to the mid-troposphere. Above the mid-troposphere (10 km) convective mass fluxes get smaller and advection plays a more important role in distributing the gases. This results in an inverted 'S' shape in the vertical profiles of $CHBr_3$ and CH_2Br_2, as discussed above. There is also a strong convection region west of Papua New Guinea/north of Australia, which transports coastal emissions to the mid and upper-troposphere.

Model mean mole fractions of $CHBr_3$ are $\simeq1.4$ ppt throughout the boundary layer (0–2 km), determined by open ocean emissions, but fall off rapidly as a function of altitude due to chemical losses. At the TTL over the study domain and during the campaign period, mean $CHBr_3$ mole fractions range 0.4–0.6 ppt mainly due to open ocean emissions. Coastal emissions are typically much larger than open ocean emissions but they play a much smaller role in observed variations throughout the troposphere except over the strong convective regions over Papua New Guinea/north of Australia. Prevailing easterly transport of gases over the region is dominated by the vast area of open ocean sources that appear to weaken the magnitude of spatially limited coastal emissions (Andrews et al., 2016; Pan et al., 2016). The vertical and spatial distributions of CH_2Br_2 mole fractions are consistent with $CHBr_3$ although they deplete less rapidly with altitude by virtue of its longer atmospheric lifetime. At the TTL, averaged over the campaign study, CH_2Br_2 mole fractions range 0.1–0.3 ppt mainly due to smaller magnitude of ocean emissions compared to $CHBr_3$. Coastal sources contribute up to 0.1 ppt of CH_2Br_2 in the TTL with the remaining originating from an open ocean source.

Figure 7 shows that ocean emissions provide the largest fractional contribution to $CHBr_3$ during CAST, typically more than 80% throughout the low to mid troposphere, with the remainder originating from emissions prior to the campaigns. This is dominated by open ocean emissions that range 50–70% of the total tracer. Coastal ocean emissions represent a smaller

contribution to CHBr$_3$ at lower altitudes, but increase their influence above 6 km in the CONTRAST data with contributions from geographical regions immediately outside the study region that reach a maximum of 60% of the total CHBr$_3$ tracer in the TTL. This results in an inverted 'S' shape observed over the vertical profile, which is described above. Island land masses generally represent only a minor contribution to the vertical profile at our model resolution, and we have excluded them from further analysis.

The ocean, in particular the open ocean, represents the largest contributions to total CH$_2$Br$_2$ over the campaign period. They typically represent 20% of the total CH$_2$Br$_2$ and reaching a maximum of 28% in the TTL for the CONTRAST measurements. Maximum contributions of coastal emission sources peak at 15% of total CH$_2$Br$_2$ tracer in the TTL, much less than for CHBr$_3$. The remaining contributions are representative of emissions prior to the campaign period.

Different CHBr$_3$ and CH$_2$Br$_2$ emission scenarios (Ordóñez et al., 2012; Ziska et al., 2013) vary with spatial distribution and magnitude of coastal and open ocean emissions, leading to uncertainties of atmospheric mixing ratios (Hossaini et al., 2013, 2016). This would have implications for results presented here, as source region mixing ratios will vary dependent on emission scenario used. We developed the age of air calculation to ascertain the influence of ocean emission regions independent of emission scenarios.

4.3 Physical Age of Air

Figure 8 shows that the air masses lofted over the open ocean study domain are responsible for the youngest air throughout the troposphere. Coastal ocean contributions are only present in the younger age profile up to 4 km. At progressively higher altitudes the probability distribution shifts towards older ages, as expected, corresponding to longer periods from the point of contact with the surface. However, at 10–13 km we see a noticeable shift towards younger ages, reflecting the peak of the convective outflow of surface air. Within the TTL, mean age increases to a value greater than the e-folding lifetime of atmospheric CHBr$_3$. However, we find using our CH$_3$I–like tracer (mean lifetime of approximately four days) that air masses can be transported to the TTL within 3–5 days but these are infrequent events so are not easily observed (Appendix B).

Assuming an indicative e-folding atmospheric lifetime τ of 24 days for CHBr$_3$ and 123 days for CH$_2$Br$_2$ we calculate that the majority of air lofted over the ocean has an age within $3\tau_{CHBr_3}$ and $1\tau_{CH_2Br_2}$. We find that 76% (92%) of oceanic emissions reach the TTL within $2\tau_{CHBr_3}$ ($3\tau_{CHBr_3}$), with 64% (88%) of open ocean emissions and 9% (50%) of coastal emissions being transported in the same time frames. The corresponding statistics for CH$_2$Br$_2$ are 99% of air lofted over the ocean reaches the TTL within $1\tau_{CH_2Br_2}$, and 99% (97%) of air emitted from the open (coastal) ocean.

Figure 9 shows that the atmospheric sampling adopted by the CAST and CONTRAST campaigns captures a similar distribution of physical ages discussed above. CAST represents a profile dominated within the boundary layer, with CONTRAST more representative of age profiles outside of the boundary layer that reflects its more extensive horizontal and vertical sampling domain. Despite intensive measurements around coastal land masses of the region, CAST did not very well capture coastal emissions. This is reflective of a model resolution that is too coarse to capture such localised effects on a sub-model-gridscale.

Figure 10 shows mixing ratios of CHBr$_3$ decreasing with altitude, but remaining fairly constant with increasing age within each altitude range. Coastal emissions are associated with the highest surface emissions but they also subjected to slow ascent

8

rates and consequently greater photochemical losses. In contrast, open ocean emissions are lower than coastal emissions but are convected more rapidly and subject to less chemical loss. Consequently, $CHBr_3$ appears to be insensitive to age. From our analysis, we found that $CHBr_3$ values are determined mainly by younger air masses from the open ocean (Figure 8). Within the TTL, higher median mole fractions are associated with the highest model convective mass flux in each age bin. The peak frequency for the mean age of air in the TTL is 48–72 days, corresponding to $3\tau_{CHBr_3}$ and median values of 0.5 pptv $CHBr_3$ from oceanic emission sources, and 0.6 pptv in high convective systems. However, less than 0.5% (2%) of air being transported to the TTL within 24–48 (48–72) days of emission are associated with high convection events. Weaker, mean convection plays an important role in more consistently transporting large mole fractions to the free troposphere that is then transported more slowly to the TTL.

To estimate the mean observed transport of $CHBr_3$ and CH_2Br_2 to the TTL we remove the calculated model bias (section 4.1), assuming this bias reflects errors in surface emissions. Figure 11 shows the resulting corrected mean vertical profiles. We calculate the uncertainties using the upper and lower limits of the bias correction, which are based on $CHBr_3$ and CH_2Br_2 data that are ±2 mean absolute deviations from the observed mean mole fractions. For $CHBr_3$ and CH_2Br_2 we find biases that range -8%–80% and 19%–43%, respectively, which we then apply to the model values throughout the atmosphere over the campaign period. We find that resulting mean model values underestimate observed $CHBr_3$ and CH_2Br_2 between 9–12 km, above the main region of convective outflow, with the observations inside the model uncertainty with the exception of CH_2Br_2. Mean model values within the TTL (above 13 km and below the local tropopause) reproduce mean observations. Based on this bias correction approach we infer a mean mole fraction and range of 0.46 (0.13–0.72) ppt and 0.88 (0.71–1.01) ppt of $CHBr_3$ and CH_2Br_2 being transported to the TTL during January and February, 2014. This is a contribution of 3.14 (1.81–4.18) pptv of Br to the TTL Br_y budget over the campaign region. This is consistent with Navarro et al. (2015) who estimate VSLS contribution over the Pacific from observations in 2013 and 2014. It estimates 3.27 ± 0.47 pptv of bromine from $CHBr_3$, CH_2Br_2 and other minor VSLS sources at the tropopause level (17 km).

5 Discussion and Concluding Remarks

We used the GEOS-Chem chemistry transport model to interpret mole fraction measurements of $CHBr_3$ and CH_2Br_2 over the Western Pacific during the CAST and CONTRAST campaigns, January–February 2014. We found that the model reproduced 30% of $CHBr_3$ measurements and 15% (45%) CAST (CONTRAST) CH_2Br_2, but had a mean positive bias of 30% for both compounds. CAST mainly sampled the marine boundary layer (70% of observations) so that biases in prior surface emissions have a greater influence on CAST than CONTRAST, which sampled throughout the troposphere.

To interpret the CAST and CONTRAST measurements of $CHBr_3$ and CH_2Br_2 we developed two new GEOS-Chem model simulations: 1) a linearised tagged simulation so that we could attribute observed changes to individual sources and geographical regions, and 2) an age of air simulation to improve understanding of the vertical transport of these compounds, acknowledging that more conventional photochemical clocks are difficult to use without more accurate boundary conditions provided by surface emission inventories.

We have three main conclusions. First, we found that open ocean emissions of $CHBr_3$ and CH_2Br_2 are primarily responsible for observed atmospheric mole fractions of these gases over the Western Pacific. Emissions from open ocean sources represent up to 70% of total $CHBr_3$, with the largest fractional contribution in the lower troposphere. Coastal ocean sources typically contribute 20% to total atmospheric $CHBr_3$ but reach a maximum of 60% in the TTL due to advection of air masses convected from areas outside the study region. Based on this model interpretation, we infer that CAST observations of $CHBr_3$, which are mainly in the lower troposphere, are dominated by open ocean sources. In contrast, CONTRAST measurements have a mix of sources, including a progressively larger contribution from coastal ocean sources in the upper troposphere. Tropospheric measurements of CH_2Br_2, which has a longer atmospheric lifetime than $CHBr_3$, are dominated by sources from before the campaign. The open ocean source typically represents only 15% of the observed variations of CH_2Br_2 emitted during the campaign region throughout the troposphere.

Second, using our age of air simulation, we find that the majority of $CHBr_3$ and CH_2Br_2 mole fractions in the TTL correspond to the youngest air masses being transported from open oceanic sources, with coastal oceans representing older air masses. Within the TTL, the highest $CHBr_3$ mole fractions are associated with the strongest convective mass flux events, but this represents only 2% of the air transported to the TTL. Weaker, slower convection processes are responsible for consistently transporting higher mole fractions to the UT and TTL. The majority of air (92%) is being transported to the TTL is within $3\tau_{CHBr_3}$ (48–72 days) corresponding to the majority of weaker convection events.

And third, we estimated the flux of $CHBr_3$ and CH_2Br_2 to the TTL using model data that have been corrected for bias. We calculated a mean and range of values 0.46 (0.13–0.72) pptv and 0.88 (0.71–1.01) pptv for $CHBr_3$ and CH_2Br_2, respectively. Together, they correspond to a total of 3.14 (1.81–4.18) pptv Br to the TTL.

References

Andrews, S. J., Carpenter, L. J., Apel, E. C., Atlas, E., Donets, V., Hopkins, J. F., Hornbrook, R. S., Lewis, A. C., Lidster, R. T., Lueb, R., Minaeian, J., Navarro, M., Punjabi, S., Riemer, D., and Schauffler, S.: A comparison of very short-lived halocarbon (VSLS) and DMS aircraft measurements in the Tropical West Pacific from CAST, ATTREX and CONTRAST, Atmospheric Measurement Techniques Discussions, 2016, 1–23, doi:10.5194/amt-2016-94, http://www.atmos-meas-tech-discuss.net/amt-2016-94/, 2016.

Aschmann, J. and Sinnhuber, B.-M.: Contribution of very short-lived substances to stratospheric bromine loading: uncertainties and constraints, Atmos. Chem. Phys., 13, 1203–1219, doi:10.5194/acp-13-1203-2013, http://www.atmos-chem-phys.net/13/1203/2013/, 2013.

Aschmann, J., Sinnhuber, B. M., Atlas, E. L., and Schauffler, S. M.: Modeling the transport of very short-lived substances into the tropical upper troposphere and lower stratosphere, Atmos. Chem. Phys. Discuss., 9, 18 511–18 543, doi:10.5194/acpd-9-18511-2009, http://www.atmos-chem-phys-discuss.net/9/18511/2009/, 2009.

Ashfold, M. J., Harris, N. R. P., Atlas, E. L., Manning, a. J., and Pyle, J. a.: Transport of short-lived species into the Tropical Tropopause Layer, Atmos. Chem. Phys., 12, 6309–6322, doi:10.5194/acp-12-6309-2012, http://www.atmos-chem-phys.net/12/6309/2012/, 2012.

Bell, N., Hsu, L., Jacob, D. J., Schultz, M. G., Blake, D. R., Butler, J. H., King, D. B., Lobert, J. M., and Maier-Reimer, E.: Methyl iodide: Atmospheric budget and use as a tracer of marine convection in global models, Journal of Geophysical Research: Atmospheres, 107, ACH 8–1–ACH 8–12, doi:10.1029/2001JD001151, http://dx.doi.org/10.1029/2001JD001151, 4340, 2002.

Carpenter, L., Reimann, S., Burkholder, J., Clerbaux, C., Hall, B., Hossaini, R., Laube, J., and Yvon-Lewis, S.: Chapter 1: Update on Ozone-Depleting Substances (ODSs) and Other Gases of Interest to the Montreal Protocol, pp. 21–125, Global Ozone Research and Monitoring Project Report, World Meteorological Organization (WMO), 2014.

Carpenter, L. J. and Liss, P. S.: On temperate sources of bromoform and other reactive organic bromine gases, J. Geophys. Res., 105, 20 539, doi:10.1029/2000JD900242, http://doi.wiley.com/10.1029/2000JD900242, 2000.

Dorf, M., Butz, a., Camy-Peyret, C., Chipperfield, M. P., Kritten, L., and Pfeilsticker, K.: Bromine in the tropical troposphere and stratosphere as derived from balloon-borne BrO observations, Atmos. Chem. Phys. Discuss., 8, 12 999–13 015, doi:10.5194/acpd-8-12999-2008, http://www.atmos-chem-phys-discuss.net/8/12999/2008/, 2008.

Fernandez, R. P., Salawitch, R. J., Kinnison, D. E., Lamarque, J.-F., and Saiz-Lopez, A.: Bromine partitioning in the tropical tropopause layer: implications for stratospheric injection, Atmospheric Chemistry and Physics, 14, 13 391–13 410, doi:10.5194/acp-14-13391-2014, http://www.atmos-chem-phys.net/14/13391/2014/, 2014.

Finch, D. P., Palmer, P. I., and Parrington, M.: Origin, variability and age of biomass burning plumes intercepted during BORTAS-B, Atmos. Chem. Phys. Discuss., 14, 8723–8752, doi:10.5194/acpd-14-8723-2014, http://www.atmos-chem-phys-discuss.net/14/8723/2014/, 2014.

Fueglistaler, S., Wernli, H., and Peter, T.: Tropical troposphere-to-stratosphere transport inferred from trajectory calculations, Journal of Geophysical Research: Atmospheres, 109, n/a–n/a, doi:10.1029/2003JD004069, http://dx.doi.org/10.1029/2003JD004069, d03108, 2004.

Fueglistaler, S., Dessler, A. E., Dunkerton, T. J., Folkins, I., Fu, Q., and Mote, P. W.: Tropical tropopause layer, Rev. Geophys., 47, RG1004, doi:10.1029/2008RG000267, http://doi.wiley.com/10.1029/2008RG000267, 2009.

Gettelman, a. and Forster, P. M. D. F.: A Climatology of the Tropical Tropopause Layer., J. Meteorol. Soc. Japan, 80, 911–924, doi:10.2151/jmsj.80.911, http://joi.jlc.jst.go.jp/JST.JSTAGE/jmsj/80.911?from=CrossRef, 2002.

Gettelman, A., Salby, M. L., and Sassi, F.: Distribution and influence of convection in the tropical tropopause region, J. Geophys. Res., 107, 4080, doi:10.1029/2001JD001048, http://doi.wiley.com/10.1029/2001JD001048, 2002.

Harris, N. R. P., Carpenter, L. J., Lee, J. D., Vaughan, G., Filus, M. T., Jones, R. L., OuYang, B., Pyle, J. A., Robinson, A. D., Andrews, S. J., Lewis, A. C., Minaeian, J., Vaughan, A., Dorsey, J. R., Gallagher, M. W., Breton, M. L., Newton, R., Percival, C. J., Ricketts, H. M. A., Baugitte, S. J.-B., Nott, G. J., Wellpott, A., Ashfold, M. J., Flemming, J., Butler, R., Palmer, P. I., Kaye, P. H., Stopford, C., Chemel, C., Boesch, H., Humpage, N., Vick, A., MacKenzie, A. R., Hyde, R., Angelov, P., Meneguz, E., and Manning, A. J.: Co-ordinated Airborne Studies in the Tropics (CAST), Bulletin of the American Meteorological Society, 0, null, doi:10.1175/BAMS-D-14-00290.1, http://dx.doi.org/10.1175/BAMS-D-14-00290.1, 2016.

Hossaini, R., Chipperfield, M. P., Monge-Sanz, B. M., Richards, N. a. D., Atlas, E., and Blake, D. R.: Bromoform and dibromomethane in the tropics: a 3-D model study of chemistry and transport, Atmos. Chem. Phys., 10, 719–735, doi:10.5194/acp-10-719-2010, http://www.atmos-chem-phys.net/10/719/2010/, 2010.

Hossaini, R., Chipperfield, M. P., Feng, W., Breider, T. J., Atlas, E., Montzka, S. a., Miller, B. R., Moore, F., and Elkins, J.: The contribution of natural and anthropogenic very short-lived species to stratospheric bromine, Atmos. Chem. Phys., 12, 371–380, doi:10.5194/acp-12-371-2012, http://www.atmos-chem-phys.net/12/371/2012/, 2012.

Hossaini, R., Mantle, H., Chipperfield, M. P., Montzka, S. A., Hamer, P., Ziska, F., Quack, B., Krüger, K., Tegtmeier, S., Atlas, E., Sala, S., Engel, A., Bönisch, H., Keber, T., Oram, D., Mills, G., Ordóñez, C., Saiz-Lopez, A., Warwick, N., Liang, Q., Feng, W., Moore, F., Miller, B. R., Marécal, V., Richards, N. A. D., Dorf, M., and Pfeilsticker, K.: Evaluating global emission inventories of biogenic bromocarbons, Atmos. Chem. Phys., 13, 11 819–11 838, doi:10.5194/acp-13-11819-2013, http://www.atmos-chem-phys.net/13/11819/2013/, 2013.

Hossaini, R., Patra, P. K., Leeson, A. A., Krysztofiak, G., Abraham, N. L., Andrews, S. J., Archibald, A. T., Aschmann, J., Atlas, E. L., Belikov, D. A., Bönisch, H., Carpenter, L. J., Dhomse, S., Dorf, M., Engel, A., Feng, W., Fuhlbrügge, S., Griffiths, P. T., Harris, N. R. P., Hommel, R., Keber, T., Krüger, K., Lennartz, S. T., Maksyutov, S., Mantle, H., Mills, G. P., Miller, B., Montzka, S. A., Moore, F., Navarro, M. A., Oram, D. E., Pfeilsticker, K., Pyle, J. A., Quack, B., Robinson, A. D., Saikawa, E., Saiz-Lopez, A., Sala, S., Sinnhuber, B.-M., Taguchi, S., Tegtmeier, S., Lidster, R. T., Wilson, C., and Ziska, F.: A multi-model intercomparison of halogenated very short-lived substances (TransCom-VSLS): linking oceanic emissions and tropospheric transport for a reconciled estimate of the stratospheric source gas injection of bromine, Atmospheric Chemistry and Physics, 16, 9163–9187, doi:10.5194/acp-16-9163-2016, http://www.atmos-chem-phys.net/16/9163/2016/, 2016.

Jones, D. B. A., Bowman, K. W., Palmer, P. I., Worden, J. R., Jacob, D. J., Hoffman, R. N., Bey, I., and Yantosca, R. M.: Potential of observations from the Tropospheric Emission Spectrometer to constrain continental sources of carbon monoxide, Journal of Geophysical Research: Atmospheres, 108, n/a–n/a, doi:10.1029/2003JD003702, http://dx.doi.org/10.1029/2003JD003702, 4789, 2003.

Ko, M. and Poulet, G.: Chapter 2: Very short-lived halogen and sulfur substances, in: Scientific Assessment of Ozone Depletion: 2002 Global Ozone Research and Monitoring Project, Report No. 47, World Meteorological Organization, Geneva, Switzerland, 2003.

Liang, Q., Stolarski, R. S., Kawa, S. R., Nielsen, J. E., Douglass, A. R., Rodriguez, J. M., Blake, D. R., Atlas, E. L., and Ott, L. E.: Finding the missing stratospheric Bry: a global modeling study of CHBr3 and CH2Br2, Atmos. Chem. Phys., 10, 2269–2286, doi:10.5194/acp-10-2269-2010, http://www.atmos-chem-phys.net/10/2269/2010/, 2010.

Liang, Q., Atlas, E., Blake, D., Dorf, M., Pfeilsticker, K., and Schauffler, S.: Convective transport of very short lived bromocarbons to the stratosphere, Atmos. Chem. Phys., 14, 5781–5792, doi:10.5194/acp-14-5781-2014, 2014.

Mackie, A. R., Palmer, P. I., Barlow, J. M., Finch, D. P., Novelli, P., and Jaegl'e, L.: Reduced Arctic air pollution due to decreasing European and North American emissions, Journal of Geophysical Research: Atmospheres, 121, 8692–8700, doi:10.1002/2016JD024923, 2016JD024923, 2016.

McLinden, C. A., Haley, C. S., Lloyd, N. D., Hendrick, F., Rozanov, A., Sinnhuber, B.-M., Goutail, F., Degenstein, D. A., Llewellyn, E. J., Sioris, C. E., Van Roozendael, M., Pommereau, J. P., Lotz, W., and Burrows, J. P.: Odin/OSIRIS observations of stratospheric BrO: Retrieval methodology, climatology, and inferred Bry, Journal of Geophysical Research: Atmospheres, 115, n/a–n/a, doi:10.1029/2009JD012488, http://dx.doi.org/10.1029/2009JD012488, d15308, 2010.

5   Montzka, S. A., Krol, M., Dlugokencky, E., Hall, B., Jöckel, P., and Lelieveld, J.: Small Interannual Variability of Global Atmospheric Hydroxyl, Science, 331, 67–69, doi:10.1126/science.1197640, http://science.sciencemag.org/content/331/6013/67, 2011.

National Geographic Data Center, NOAA: 2-minute Gridded Global Relief Data (ETOPO2) v2., doi:10.7289/v5j1012q, National Oceanic and Atmospheric Administration, Accessed: 2015-07-25, 2006.

Navarro, M. A., Atlas, E. L., Saiz-Lopez, A., Rodriguez-Lloveras, X., Kinnison, D. E., Lamarque, J.-F., Tilmes, S., Filus, M., Harris, N.

10   R. P., Meneguz, E., Ashfold, M. J., Manning, A. J., Cuevas, C. A., Schauffler, S. M., and Donets, V.: Airborne measurements of organic bromine compounds in the Pacific tropical tropopause layer, Proceedings of the National Academy of Sciences, 112, 13 789–13 793, doi:10.1073/pnas.1511463112, http://www.pnas.org/content/112/45/13789.abstract, 2015.

Ordóñez, C., Lamarque, J.-F., Tilmes, S., Kinnison, D. E., Atlas, E. L., Blake, D. R., Sousa Santos, G., Brasseur, G., and Saiz-Lopez, a.: Bromine and iodine chemistry in a global chemistry-climate model: description and evaluation of very short-lived oceanic sources, Atmos.

15   Chem. Phys., 12, 1423–1447, doi:10.5194/acp-12-1423-2012, http://www.atmos-chem-phys.net/12/1423/2012/, 2012.

Palmer, P. I., Jacob, D. J., Jones, D. B. A., Heald, C. L., Yantosca, R. M., Logan, J. A., Sachse, G. W., and Streets, D. G.: Inverting for emissions of carbon monoxide from Asia using aircraft observations over the western Pacific, Journal of Geophysical Research: Atmospheres, 108, n/a–n/a, doi:10.1029/2003JD003397, http://dx.doi.org/10.1029/2003JD003397, 8828, 2003.

Pan, L. L., Paulik, L. C., Honomichl, S. B., Munchak, L. A., Bian, J., Selkirk, H. B., and Vömel, H.: Identification of the tropical

20   tropopause transition layer using the ozone-water vapor relationship, Journal of Geophysical Research: Atmospheres, 119, 3586–3599, doi:10.1002/2013JD020558, http://dx.doi.org/10.1002/2013JD020558, 2013JD020558, 2014.

Pan, L. L., Atlas, E. L., Salawitch, R. J., Honomichl, S. B., Bresch, J. F., Randel, W. J., Apel, E. C., Hornbrook, R. S., Weinheimer, A. J., Anderson, D. C., Andrews, S. J., Baidar, S., Beaton, S. P., Campos, T. L., Carpenter, L. J., Chen, D., Dix, B., Donets, V., Hall, S. R., Hanisco, T. F., Homeyer, C. R., Huey, L. G., Jensen, J. B., Kaser, L., Kinnison, D. E., Koenig, T. K., Lamarque, J.-F., Liu, C., Luo,

25   J., Luo, Z. J., Montzka, D. D., Nicely, J. M., Pierce, R. B., Riemer, D. D., Robinson, T., Romashkin, P., Saiz-Lopez, A., Schauffler, S., Shieh, O., Stell, M. H., Ullmann, K., Vaughan, G., Volkamer, R., and Wolfe, G.: The Convective Transport of Active Species in the Tropics (CONTRAST) Experiment, Bulletin of the American Meteorological Society, 0, null, doi:10.1175/BAMS-D-14-00272.1, http://dx.doi.org/10.1175/BAMS-D-14-00272.1, 2016.

Quack, B. and Wallace, D. W. R.: Air-sea flux of bromoform: Controls, rates, and implications, Global Biogeochem. Cycles, 17, 23 1–27,

30   doi:10.1029/2002GB001890, http://doi.wiley.com/10.1029/2002GB001890, 2003.

Quack, B., Atlas, E., Petrick, G., and Wallace, D. W. R.: Bromoform and dibromomethane above the Mauritanian upwelling: Atmospheric distributions and oceanic emissions, J. Geophys. Res., 112, D09 312, doi:10.1029/2006JD007614, http://doi.wiley.com/10.1029/2006JD007614, 2007.

Salawitch, R. J., Canty, T., Kurosu, T., Chance, K., Liang, Q., da Silva, A., Pawson, S., Nielsen, J. E., Rodriguez, J. M., Bhartia, P. K., Liu,

35   X., Huey, L. G., Liao, J., Stickel, R. E., Tanner, D. J., Dibb, J. E., Simpson, W. R., Donohoue, D., Weinheimer, A., Flocke, F., Knapp, D., Montzka, D., Neuman, J. A., Nowak, J. B., Ryerson, T. B., Oltmans, S., Blake, D. R., Atlas, E. L., Kinnison, D. E., Tilmes, S., Pan, L. L., Hendrick, F., Van Roozendael, M., Kreher, K., Johnston, P. V., Gao, R. S., Johnson, B., Bui, T. P., Chen, G., Pierce, R. B.,

Crawford, J. H., and Jacob, D. J.: A new interpretation of total column BrO during Arctic spring, Geophysical Research Letters, 37, n/a–n/a, doi:10.1029/2010GL043798, http://dx.doi.org/10.1029/2010GL043798, l21805, 2010.

Sander, S., Friedl, R., Barker, J., Golden, D., Kurylo, M., Wine, P., Abbatt, J., Burkholder, J., Kolb, C., Moortgat, G., Huie, R., and Orkin, V.: Chemical Kinetics and Photochemical Data for Use in Atmospheric Studies, Evaluation Number 17, JPL Publication 10–6, Jet Propulsion Laboratory, http://jpldataeval.jpl.nasa.gov, 2011.

Sinnhuber, B.-M. and Folkins, I.: Estimating the contribution of bromoform to stratospheric bromine and its relation to dehydration in the tropical tropopause layer, Atmos. Chem. Phys., 6, 4755–4761, doi:10.5194/acp-6-4755-2006, http://www.atmos-chem-phys.net/6/4755/2006/, 2006.

Sinnhuber, B.-M., Arlander, D. W., H, B., Burrows, J. P., Chipperfield, M. P., Enell, C.-F., Frieb, U., Hendrick, F., Johnston, P. V., Jones, R. L., Kreher, K., Mohamed-Tahrin, N., Muller, R., Pfeilsticker, K., Platt, U., Pommereau, J.-P., Pundt, I., Richter, A., South, A. M., Tornkvist, K. K., Van Roozendael, M., Wagner, T., and Wittrock, F.: Comparison of measurements and model calculations of stratospheric bromine monoxide, J. Geophys. Res., 107, 4398, doi:10.1029/2001JD000940, http://doi.wiley.com/10.1029/2001JD000940, 2002.

Sinnhuber, B.-M., Rozanov, A., Sheode, N., Afe, O. T., Richter, A., Sinnhuber, M., Wittrock, F., Burrows, J. P., Stiller, G. P., von Clarmann, T., and Linden, A.: Global observations of stratospheric bromine monoxide from SCIAMACHY, Geophysical Research Letters, 32, n/a–n/a, doi:10.1029/2005GL023839, http://dx.doi.org/10.1029/2005GL023839, l20810, 2005.

Sioris, C. E., Kovalenko, L. J., McLinden, C. A., Salawitch, R. J., Van Roozendael, M., Goutail, F., Dorf, M., Pfeilsticker, K., Chance, K., von Savigny, C., Liu, X., Kurosu, T. P., Pommereau, J.-P., Bösch, H., and Frerick, J.: Latitudinal and vertical distribution of bromine monoxide in the lower stratosphere from Scanning Imaging Absorption Spectrometer for Atmospheric Chartography limb scattering measurements, Journal of Geophysical Research: Atmospheres, 111, n/a–n/a, doi:10.1029/2005JD006479, http://dx.doi.org/10.1029/2005JD006479, d14301, 2006.

Tegtmeier, S., Krüger, K., Quack, B., Atlas, E. L., Pisso, I., Stohl, a., and Yang, X.: Emission and transport of bromocarbons: from the West Pacific ocean into the stratosphere, Atmos. Chem. Phys., 12, 10 633–10 648, doi:10.5194/acp-12-10633-2012, http://www.atmos-chem-phys.net/12/10633/2012/, 2012.

Warwick, N. J., Pyle, J. a., Carver, G. D., Yang, X., Savage, N. H., O'Connor, F. M., and Cox, R. a.: Global modeling of biogenic bromocarbons, J. Geophys. Res., 111, D24 305, doi:10.1029/2006JD007264, http://doi.wiley.com/10.1029/2006JD007264, 2006.

WMO: Scientific Assessment of Ozone Depletion: 2006, Global Ozone Research and Monitoring Project - Report No. 50, 572pp., Tech. rep., World Meteorological Organization, Geneva, 2007.

Zhou, X. L., Geller, M. A., and Zhang, M.: Temperature Fields in the Tropical Tropopause Transition Layer, Journal of Climate, 17, 2901–2908, doi:10.1175/1520-0442(2004)017<2901:TFITTT>2.0.CO;2, 2004.

Ziska, F., Quack, B., Abrahamsson, K., Archer, S. D., Atlas, E., Bell, T., Butler, J. H., Carpenter, L. J., Jones, C. E., Harris, N. R. P., Hepach, H., Heumann, K. G., Hughes, C., Kuss, J., Krüger, K., Liss, P., Moore, R. M., Orlikowska, a., Raimund, S., Reeves, C. E., Reifenhäuser, W., Robinson, a. D., Schall, C., Tanhua, T., Tegtmeier, S., Turner, S., Wang, L., Wallace, D., Williams, J., Yamamoto, H., Yvon-Lewis, S., and Yokouchi, Y.: Global sea-to-air flux climatology for bromoform, dibromomethane and methyl iodide, Atmos. Chem. Phys., 13, 8915–8934, doi:10.5194/acp-13-8915-2013, http://www.atmos-chem-phys.net/13/8915/2013/, 2013.

Table 1. Mean measurement statistics for $CHBr_3$ and CH_2Br_2 mole fraction data as a function of altitude for CAST and CONTRAST aircraft campaigns. $\overline{x}$, σ, and n denote the mean value, the standard deviation, and the number of data points used to determine the statistics.

Altitude	$CHBr_3$		CH_2Br_2	
	CAST	CONTRAST	CAST	CONTRAST
km	$\overline{x}$, 1σ, & range [ppt]; n	$\overline{x}$, 1σ, & range [ppt]; n	$\overline{x}$, 1σ, & range [ppt]	$\overline{x}$, 1σ, & range [ppt]
0−2	0.95, 0.45, 0.42−3.00; 502	0.89, 0.23, 0.51−1.55; 75	1.01, 0.13, 0.72−1.64	1.07, 0.11, 0.83−1.27
2−4	0.61, 0.16, 0.29−0.98; 147	0.62, 0.18, 0.29−1.24; 48	0.91, 0.05, 0.73−1.06	0.94, 0.09, 0.78−1.13
4−6	0.44, 0.17, 0.03−0.79; 59	0.56, 0.18, 0.20−1.12; 65	0.88, 0.06, 0.69−1.00	0.91, 0.09, 0.73−1.12
6−8	0.38, 0.25, 0.02−0.81, 53	0.60, 0.20, 0.24−1.01; 43	0.85, 0.11, 0.63−1.06	0.90, 0.10, 0.70−1.06
8−10	0.48, 0.34, 0.14−0.82; 2	0.62, 0.17, 0.24−1.00; 43	0.90, 0.13, 0.77−1.03	0.93, 0.09, 0.72−1.07
10−13	–	0.59, 0.25, 0.00−1.38; 130	–	0.87, 0.19, 0.21−1.10
TTL	–	0.48, 0.16, 0.18−1.17; 280	–	0.86, 0.08, 0.64−1.06

Table 2. Location and code of NOAA/ESRL ground-based stations.

Station	Name	Lat	Lon
ALT	Alert, NW Territories, Canada	82.5°N	62.3°W
SUM	Summit, Greenland	72.6°N	38.4°W
BRW	Pt. Barrow, Alaska, USA	71.3°N	156.6°W
MHD	Mace Head, Ireland	53.0°N	10.0°W
LEF	Wisconsin, USA	45.6°N	90.2°W
HFM	Massachusetts, USA	42.5°N	72.2°W
THD	Trinidad Head, USA	41.0°N	124.0°W
NWR	Niwot Ridge, Colorado, USA	40.1°N	105.6°W
KUM	Cape Kumukahi, Hawaii, USA	19.5°N	154.8°W
MLO	Mauna Loa, Hawaii, USA	19.5°N	155.6°W
SMO	Cape Matatula, American Samoa	14.3°S	170.6°W
CGO	Cape Grim, Tasmania, Australia	40.7°S	177.8°E
PSA	Palmer Station, Antarctica	64.6°S	64.0°W
SPO	South Pole	90.0°N	–

Table 3. Seasonal mean statistics for NOAA ground station sites (Table 2) showing Pearson correlations, r^2, between observed and climatological monthly mean $CHBr_3$ and CH_2Br_2 mole fraction data, and corresponding model biases.

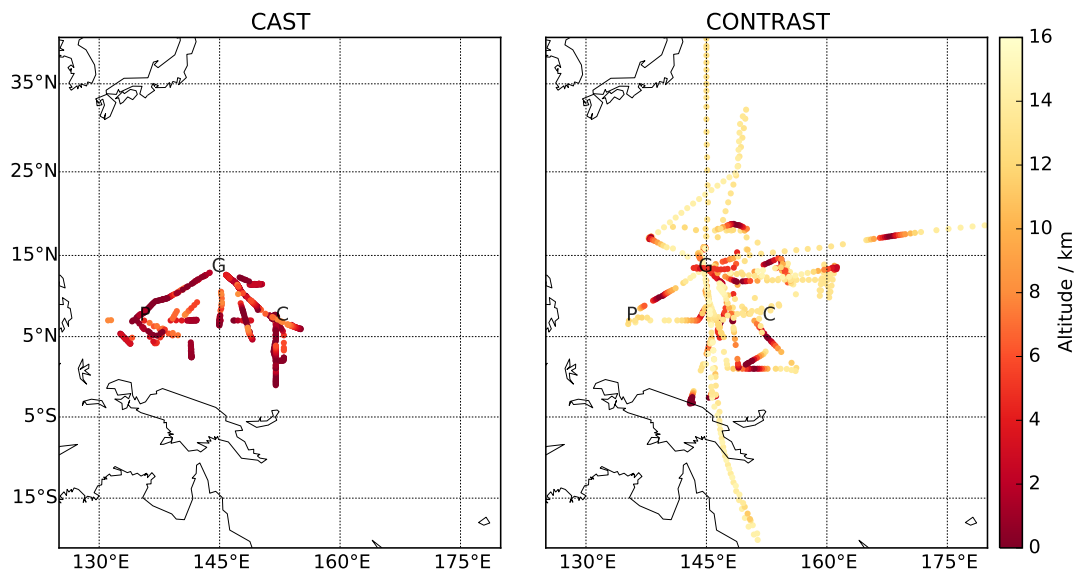|	CHBr$_3$				CH$_2$Br$_2$			
	DJF	MAM	JJA	SON	DJF	MAM	JJA	SON
Station	r^2, %bias	r^2, %bias	r^2, %bias	r^2, %bias	r^2, %bias	r^2, %bias	r^2, %bias	r^2, %bias
ALT	0.00, 3.8	0.55, 0.1	0.05, 5.5	0.43, 19.3	0.09, 12.4	0.21, 0.0	0.23, 10.0	0.31, 21.0
SUM	0.05, 25.1	0.01, -17.1	0.23, -12.0	0.54, 20.6	0.06, -2.7	0.15, -13.0	0.15, 4.8	0.60, 7.0
BRW	0.00, -41.3	0.52, -30.2	0.13, -26.5	0.80, -26.5	0.15, 9.5	0.07, -8.7	0.00, -4.4	0.14, 15.9
MHD	0.00, -40.8	0.18, -72.4	0.04, -80.6	0.08, -61.2	0.05, -20.5	0.11, -35.9	0.14, -42.7	0.03, -16.8
LEF	0.03, 45.7	0.01, 15.5	0.03, 39.3	0.73, 51.2	0.17, 13.4	0.25, 3.1	0.44, 18.2	0.66, 20.8
HFM	0.06, 52.2	0.01, 30.1	0.15, 46.9	0.38, 52.3	0.03, 20.0	0.06, 9.3	0.22, 27.1	0.45, 25.7
THD	0.19, 55.3	0.15, 15.8	0.36, 11.7	0.17, 40.2	0.09, 16.9	0.06, 0.9	0.01, 8.6	0.06, 18.0
NWR	0.02, 43.3	0.49, 25.9	0.01, 21.8	0.31, 38.7	0.20, 2.3	0.55, 4.9	0.40, 11.9	0.55, 14.7
KUM	0.00, 20.2	0.37, -1.9	0.05, 0.9	0.01, 6.8	0.25, -0.3	0.50, 4.4	0.47, 15.6	0.38, 9.9
MLO	0.18, 61.9	0.60, 60.3	0.02, 65.1	0.58, 64.7	0.14, 14.8	0.32, 15.2	0.21, 22.8	0.27, 25.0
SMO	0.23, 8.2	0.02, -4.9	0.04, 3.0	0.11, 4.7	0.39, 6.9	0.38, -0.9	0.19, -0.2	0.09, 5.6
CGO	0.23, -39.0	0.01, -12.8	0.05, 7.7	0.00, -19.6	0.13, -8.7	0.13, -1.6	0.04, -1.4	0.12, -9.5
PSA	0.19, -13.9	0.25, 26.4	0.01, 31.7	0.05, -1.9	0.00, -1.7	0.29, 11.7	0.15, 10.3	0.05, -2.0
SPO	0.50, 6.6	0.12, 6.7	0.07, 19.2	0.11, -7.3	0.01, 4.8	0.06, 4.6	0.11, 3.7	0.00, -0.6

Figure 1. Measurement distribution of $CHBr_3$ and CH_2Br_2 mole fractions from the CAST (left) and CONTRAST (right) aircraft campaigns as a function of altitude (km). Relevant island waypoints are shown inset: Guam (G), Palau (P), and Chuuk (C).
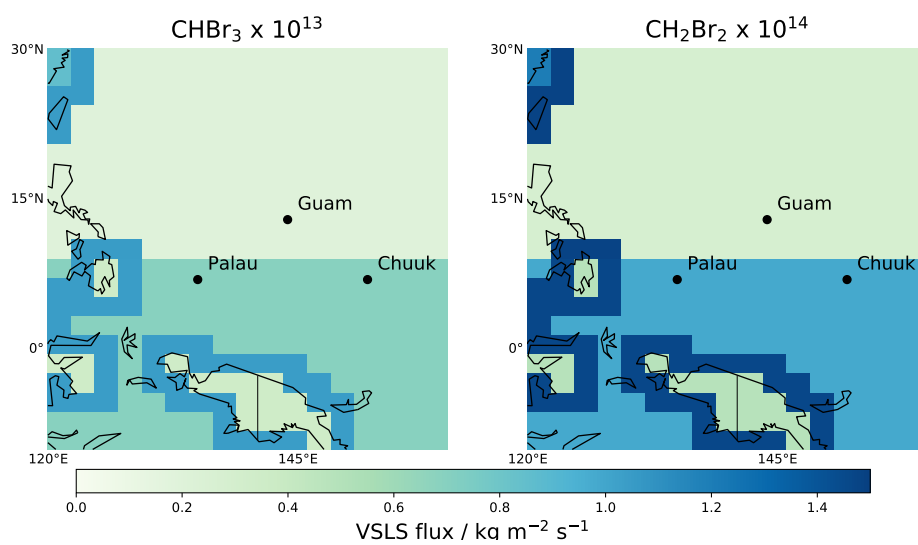
Figure 2. Surface emissions of CHBr$_3$ (10^{13}kg/m^2/s) and CH$_2$Br$_2$ (10^{14}kg/m^2/s) taken from Liang et al. (2010) for the time and study domain of the CAST and CONTRAST campaigns.
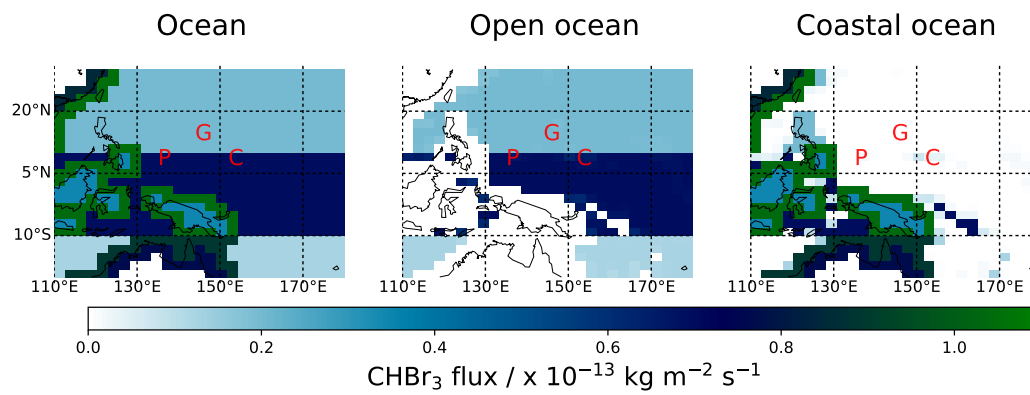
Figure 3. Flux of CHBr$_3$ from total, open, and coastal ocean tracers. Relevant island waypoints are shown inset: Guam (G), Palau (P), and Chuuk (C).
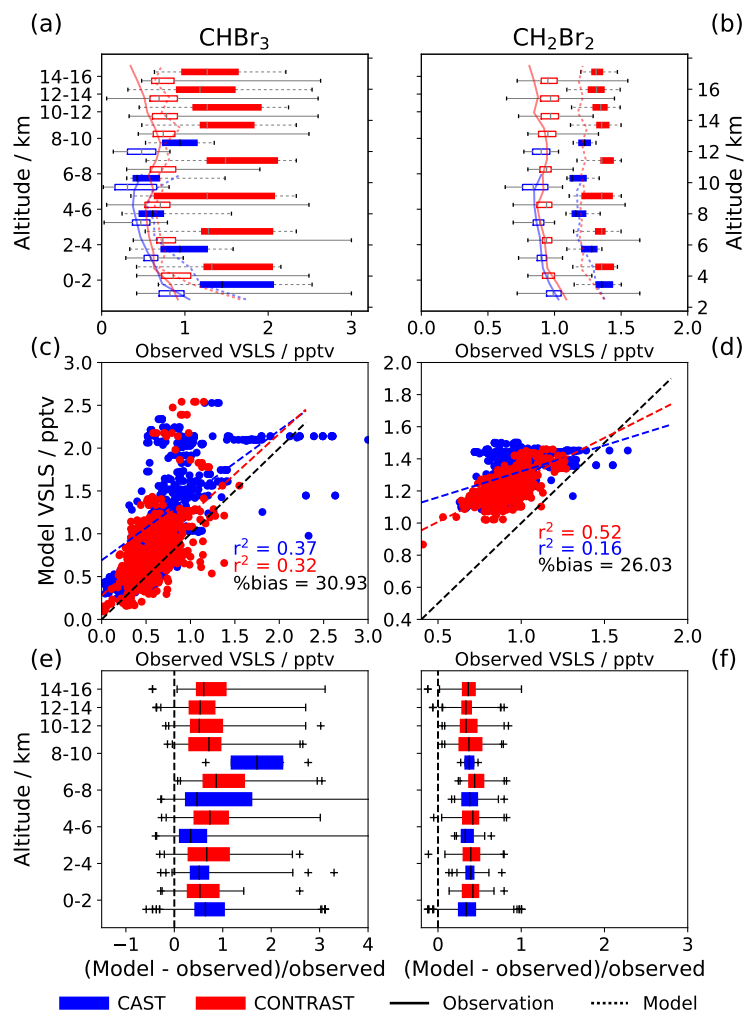
Figure 4. Comparison of model and observed (left panels) $CHBr_3$ (pptv) and (right panels) CH_2Br_2 (pptv) mole fraction data for CAST (denoted by blue) and CONTRAST (denoted by red). Top panels describe the comparison between model (dotted line) and observed (solid line) values as a box and whiskers plot on 2-km altitude bins. The middle panel describes the model and data comparison as a scatterplot. Pearson correlations (r^2) and percentage biases are shown inset. Black, red, and blue dashed lines denote the 1:1 line, and the best fit linear models for CONTRAST and CAST, respectively. The bottom panel show the relative model error, described as a box and whiskers plot on 2-km altitude bins. The vertical dashed line denote the zero error line.
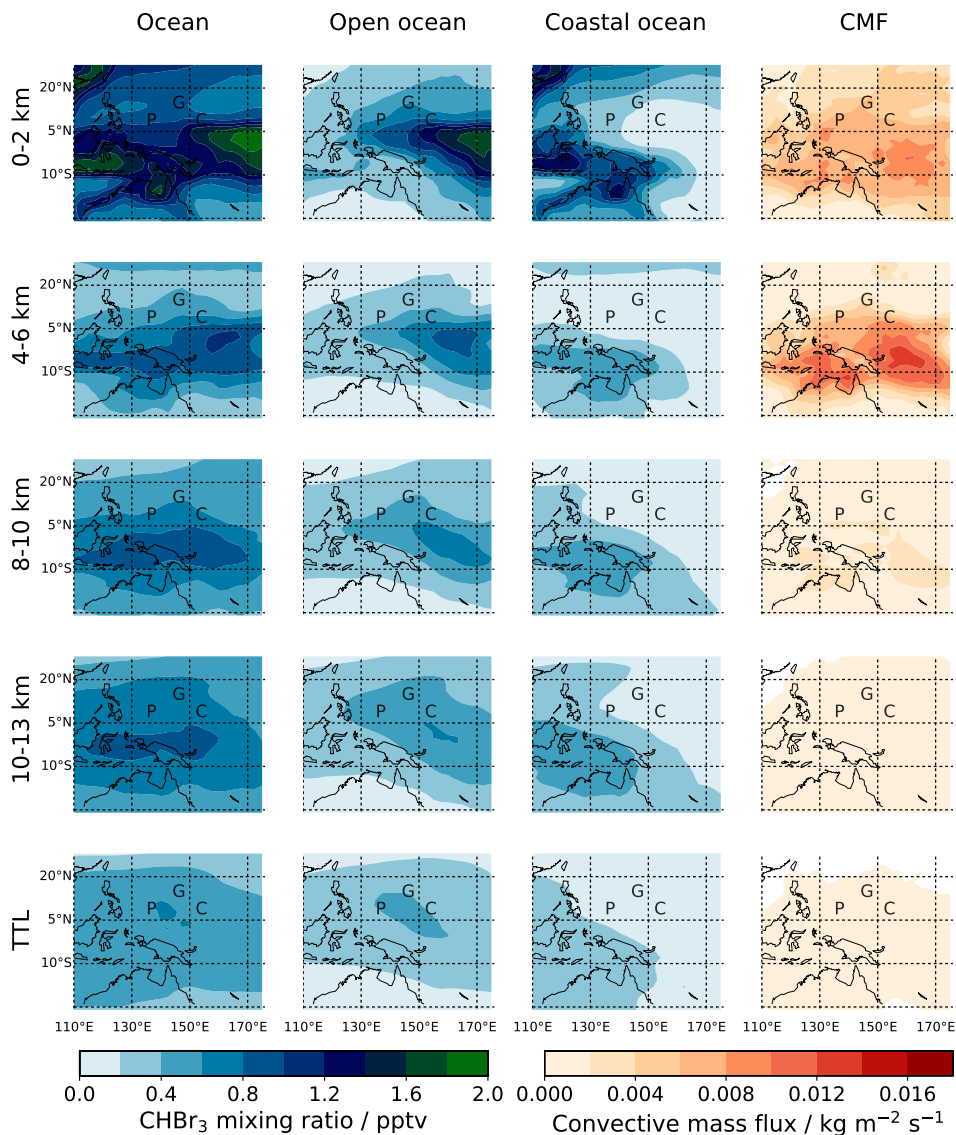
Figure 5. Model mole fractions (pptv) of CHBr$_3$ over the study domain as a function of altitude, averaged between 18/01/14 and 28/02/14, from the total (column 1), open (column 2) and coastal ocean (column 3) tagged tracers. The corresponding mean model convective mass flux (kg/m^2/s) is shown in column 4. Tagged tracers are averaged from 2-hour fields and convective mass fluxes are averaged from daily fields.
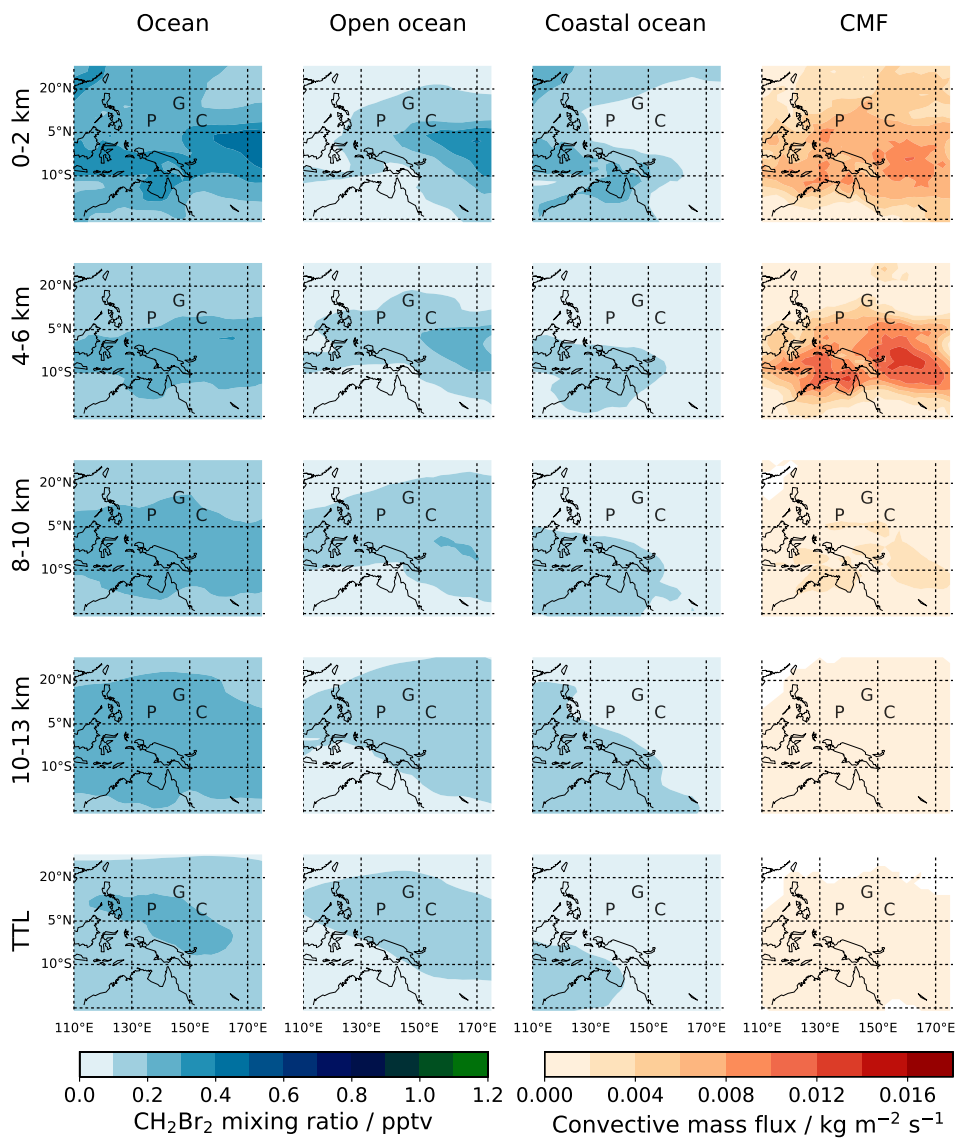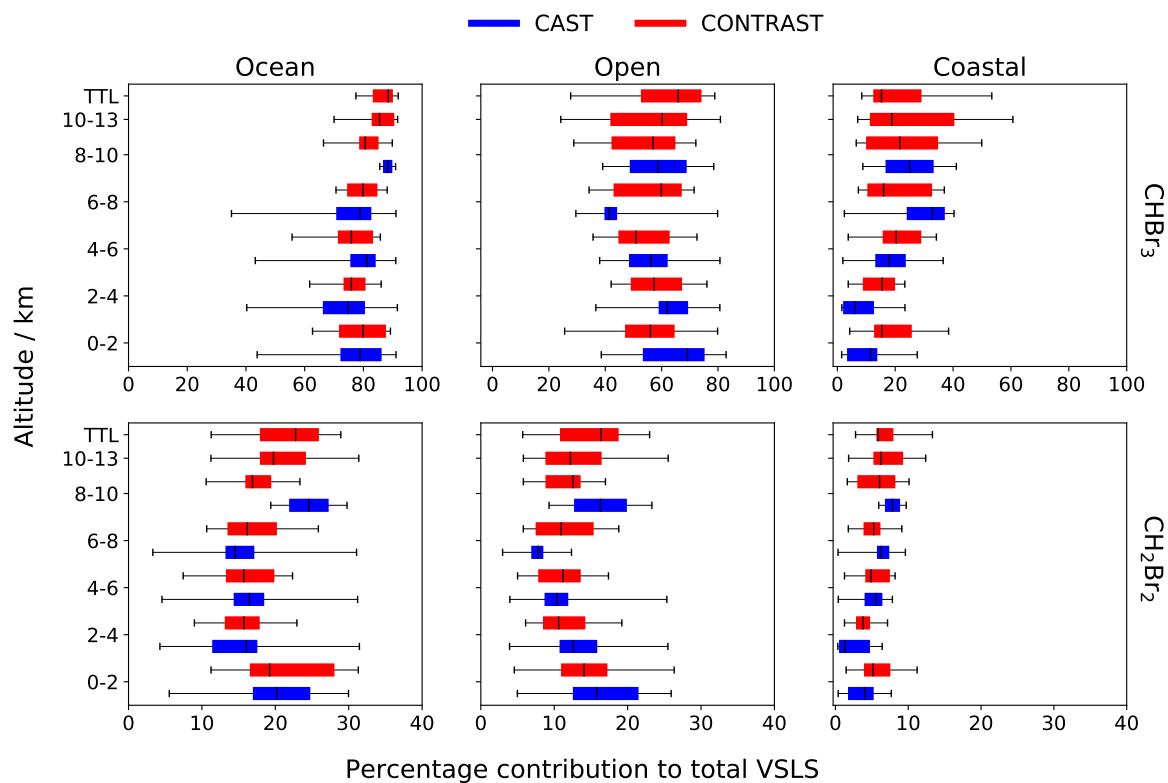
Figure 6. As Figure 5 but for CH_2Br_2 (pptv).

Figure 7. The percentage contributions from total ocean, open oceans, and coastal oceans to total (top) CHBr$_3$ and (bottom) CH$_2$Br$_2$ described as a box and whiskers plot on 1-km altitude bins.
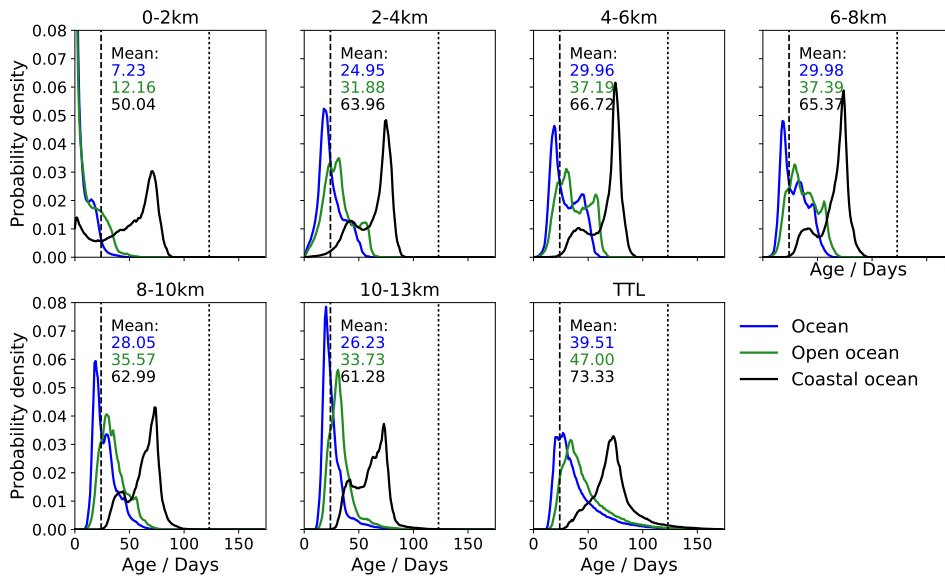
Figure 8. Probability density functions of the age of air *A* for (blue) total ocean, (green) open oceans, and (black) coastal ocean tracers, described as 2-km altitude regions from the surface to the TTL (13 km to the tropopause) averaged over the whole study domain between 18/01/2014–28/02/2014.
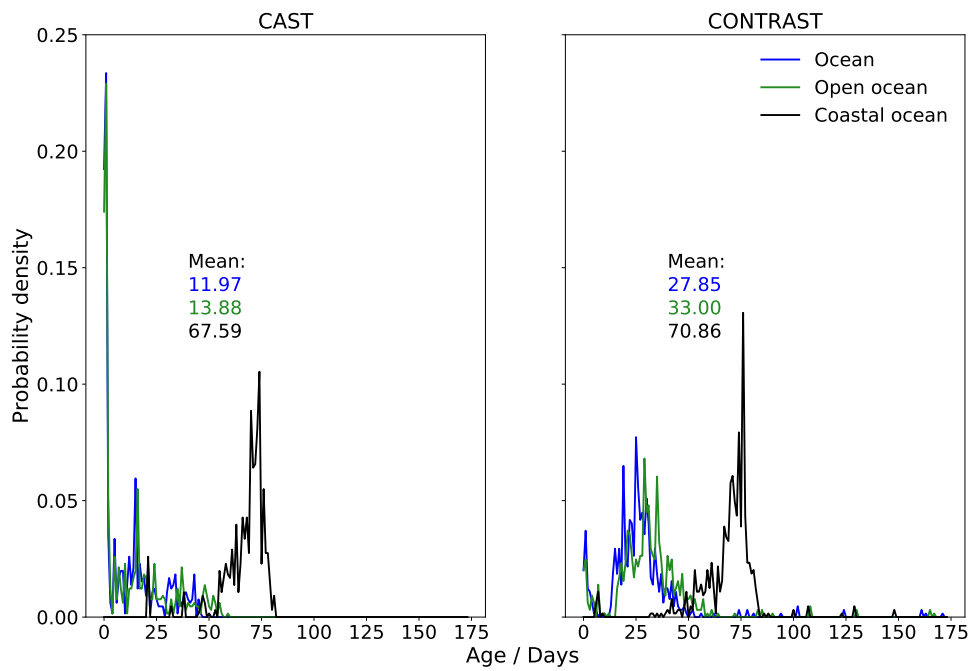
Figure 9. As Figure 8 but sampled along CAST and CONTRAST flight tracks.
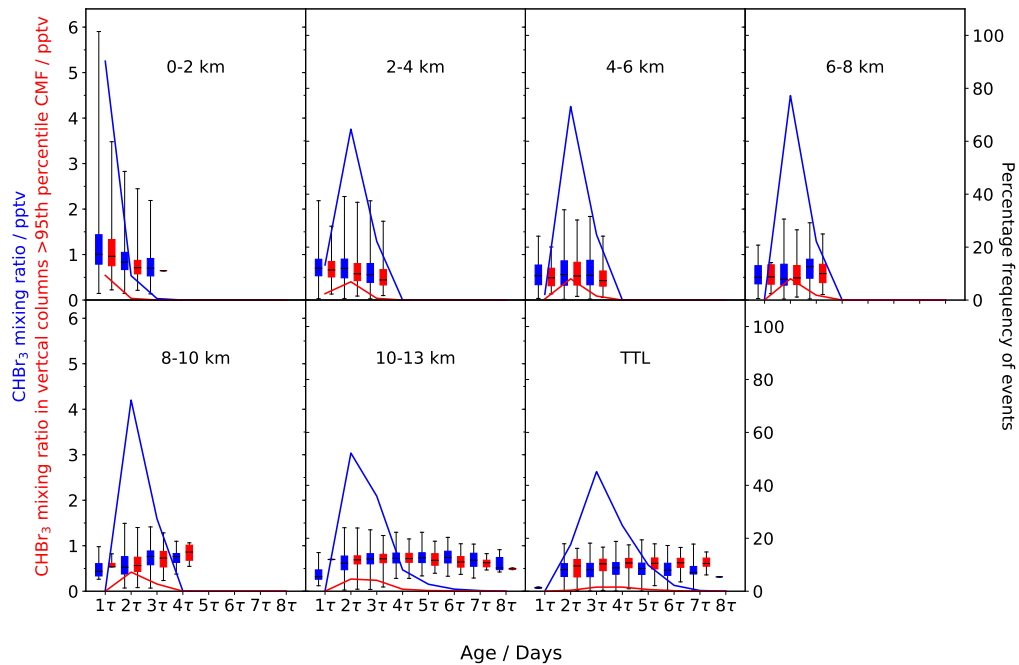
Figure 10. Box and whiskers plot of model CHBr$_3$ mole fractions from the entire ocean tracer as a function of 2 km altitude intervals and a nominal 24-day e-folding lifetime (τ). Data are averaged over 18/01/2014–28/02/2014 and over 10°S-30°N, 125-175°E. Blue values correspond to results determined by all available data, and red values correspond to results determined by convective mass fluxes >95th percentile. Solid lines denotes the percentage of occurrence rate over the period and region denoted above. Percentage of occurrence rate refers to how often air masses fall within the specified age range.
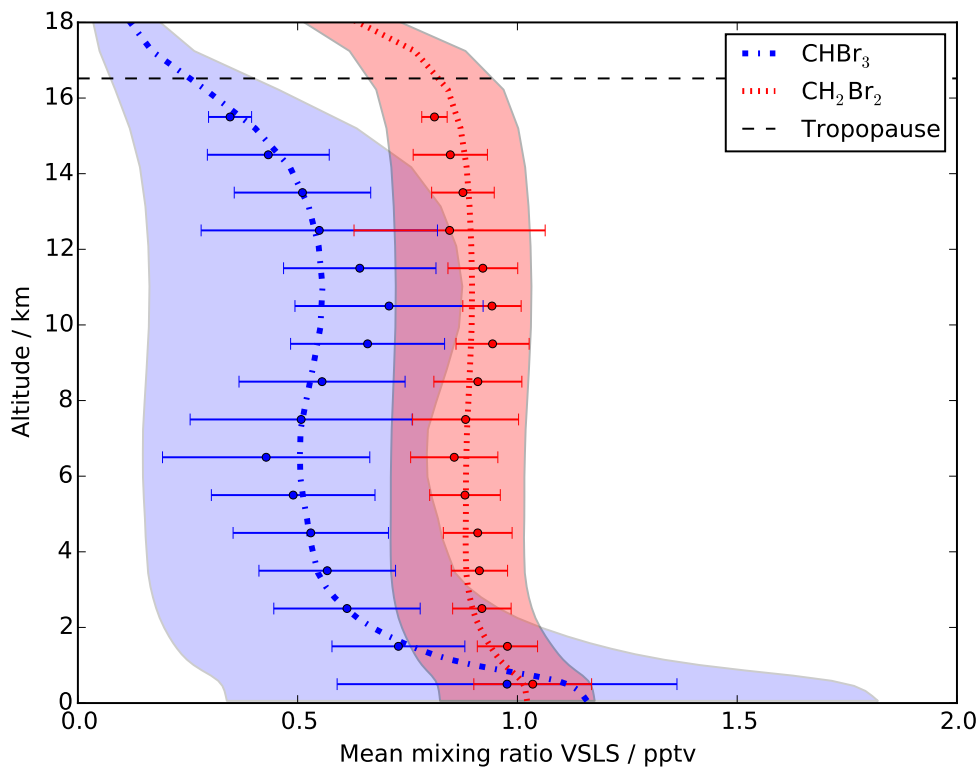
Figure 11. Observed (solid circles) and model (dashed-dot line) mean mole fractions of CHBr$_3$ (blue) and CH$_2$Br$_2$ (red) as a function of altitude, January–February 2014. The solid horizontal lines associated with each mean observation denotes the range about that mean. The coloured envelopes associated with the model denote the uncertainty based on the bias correction as described in the main text. The black horizontal dashed line denotes the mean model tropopause of 16.5 km.

Appendix A: Model Evaluation Using NOAA Surface Mole Fraction Measurements

Figure A.1 shows that the majority of station sites have a positive model bias with magnitude varying depending on location. Mid-latitude stations (LEF–NWR) have similar bias values of 30–40% (10–20%) for $CHBr_3$ (CH_2Br_2). At the tropical sites, which are comparable with the campaign region, the model bias varies strongly depending on location. This variability will

5   represent the large variability of convective events over the region, as well as the aforementioned errors in model emissions. KUM and MLO both sit on Hawaii, with KUM and SMO being a near surface coastal station and MLO sitting at an elevated altitude of 3397 m. Model bias calculated for MLO (60%) is much greater than the other two near surface sites (<10%), however it gives the strongest annual correlation with r^2 values of 0.75 (0.55) for $CHBr_3$ (CH_2Br_2). All coastal sites (with exception of ALT) near emission sources have low r^2 values (<0.4) suggesting the model does not capture local variations

10   in emissions well. This is also representative of the variation of convection events over the tropical region being represented within the model.

Seasonal variations within model bias and correlations of $CHBr_3$ and CH_2Br_2 are shown in Table 3. The campaign season of DJF is poorly constrained within the model at all sites with an $r^2 < 0.5$ for both gases. The annual correlation at sites appears to be dominated by other seasons. Within the tropical stations, model bias increases from the annual at KUM to around 20%

15   with no correlation to observed values. MLO and SMO show a similar seasonal bias to the annual indicating the effect to be local to the KUM station site.

Figure A.2 shows that the model reproduces the seasonal cycle well at all three sites. The emissions at these sites are not scaled seasonally, the phase is representative of the chemistry at these sites. The shorter lived $CHBr_3$ profile is dominates by its loss from photolysis whereas the CH_2Br_2 cycle is dominated by oxidation with OH. The amplitude of the seasonal cycle is

20   overestimated in $CHBr_3$ at MLO, and to a lesser extent KUM. This can be indicative of local biases within photolysis loss rates and/or emissions. The same effect is not shown within the CH_2Br_2 suggesting there is not a similar problem associated with OH fields. This is concurrent with a recent multi-decadal analysis of carbon monoxide (Mackie et al., 2016) at higher northern latitudes does not support a major problem with similar monthly 3-D fields of OH.
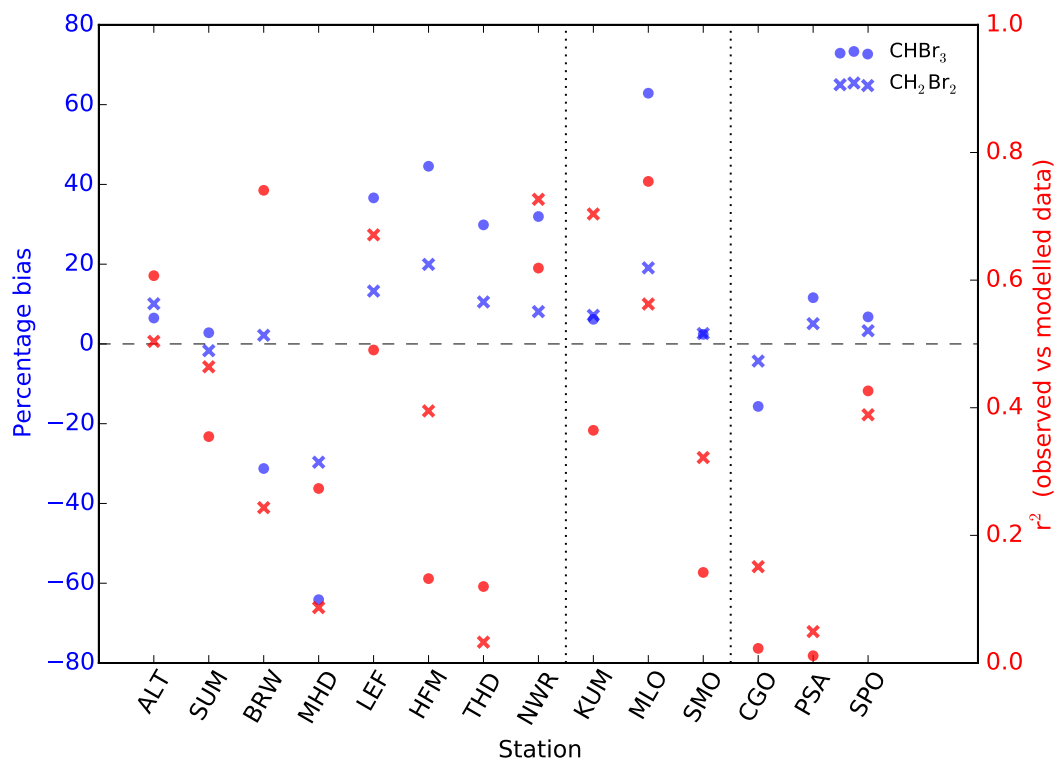
Figure A.1. Mean annual percentage model bias (blue) calculated at NOAA ground station sites (Table 2) for $CHBr_3$ (dots) and CH_2Br_2 (crosses). The horizontal dashed line denotes zero bias. The right-hand-side y axis describes the ability of the model to reproduce observed variations (r^2) (red). The vertical dotted lines define the tropical stations.
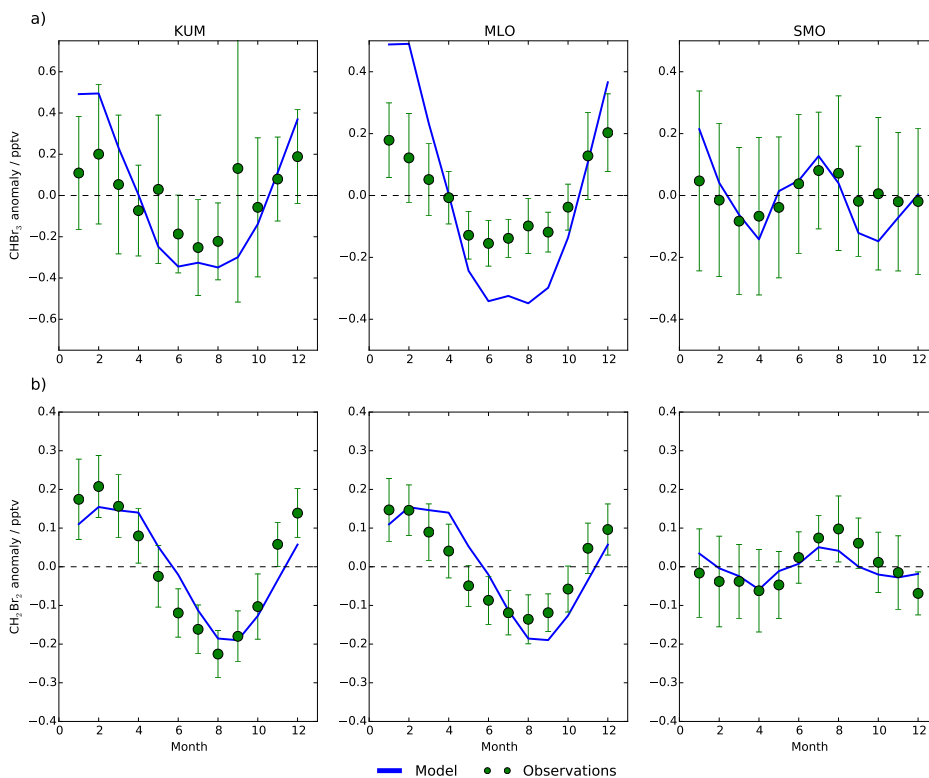
Figure A.2. Observed (green) and model (blue) mole fractions of (a) CHBr$_3$ and (b) CH$_2$Br$_2$ at tropical NOAA sites. The seasonal cycle is shown as the climatological monthly mean anomaly calculated by subtracting the annual mean from the climatological monthly mean (pptv). Horizontal bars on observed values denote $\pm 1\sigma$.

Appendix B: Evaluation of Model Convection

To evaluate model convection over the marine environment during the CAST and CONTRAST campaigns, we developed a short-lived tagged tracer simulation with an e-folding lifetime comparable to CH$_3$I, as described in section 3.

We emitted CH$_3$I at an equilibrium mole fraction of 1 pptv over ocean regions and applied an atmospheric e-folding lifetime
5   of four days similar to that CH$_3$I in the tropics (Carpenter et al., 2014). We can then use the model mole fraction to determine the effective mean age of air parcels throughout the troposphere, and to compare the qualitatively to observed CH$_3$I values collected during the CONTRAST campaign.

Figure B.1 shows that the model can generally reproduce the quantitative vertical distribution of CH$_3$I: a decrease from the surface source up to an altitude of 10–11 km. Above this, there is a 1-2 km altitude region where values are higher than those
10   in the free troposphere, suggestive of outflow from convection. As expected, the youngest air masses are close to the surface

with the ages as young as 5–6 days in the upper troposphere. These ages are indicative of fast convective transport but they are not as young as would be expected from some of the highest observed mole fractions, which are likely due to faster, sub-grid scale, convective transport.

Figure B.2 shows that the model captures infrequent fast, large-scale convective transport over the study domain, with ages as young as 3–4 days reaching the upper troposphere. One metric to describe the convective transport is the marine convection index (MCI), following Bell et al. (2002): the ratio of mean upper tropospheric CH_3I (8–12 km) to lower tropospheric CH_3I (0–2.5 km). The CONTRAST observations have an MCI of 0.38 and the corresponding model MCI sampled for these observations is 0.19. The MCI for the model domain for the duration of CONTRAST is 0.28. These values are consistent with those found in Bell et al. (2002) over a similar Pacific regions.

Overall, we find that the model describes the mean convective flow over the region and can capture instances of rapid, large-scale convective transport. Differences in the MCI suggest a significant role for rapid, sub-grid scale vertical transport that are not captured by our coarse model resolution.
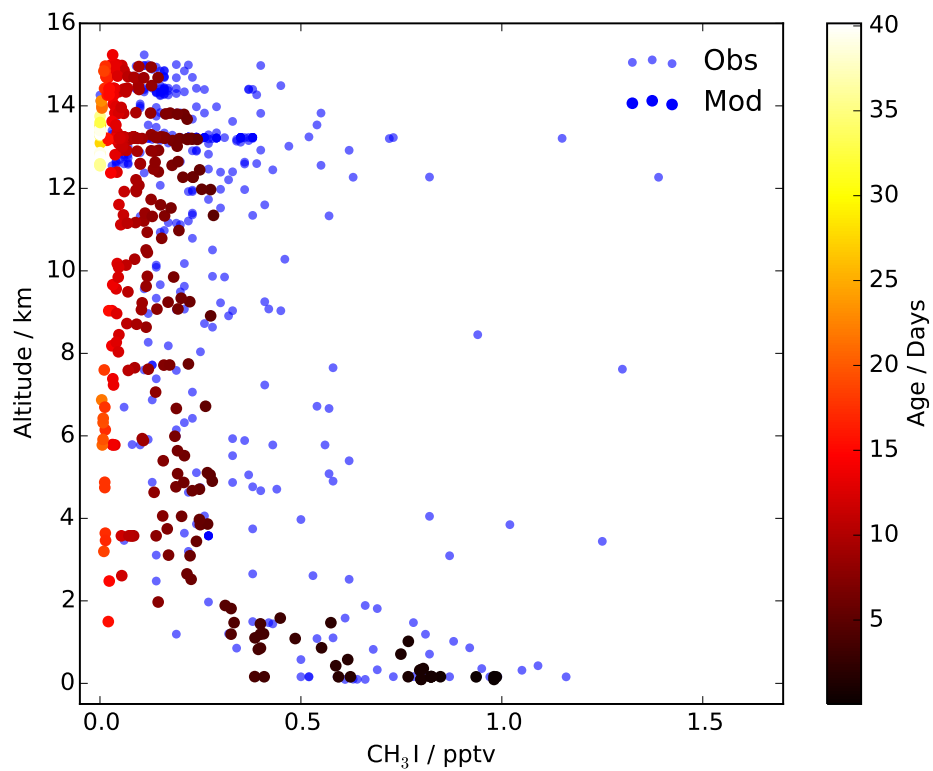
Figure B.1. Vertical profiles of observed (blue) and synthetic (coloured as a function of age) CH₃I mole fraction data sampled along flight tracks corresponding to AWAS samples collected during CONTRAST as a function of altitude.
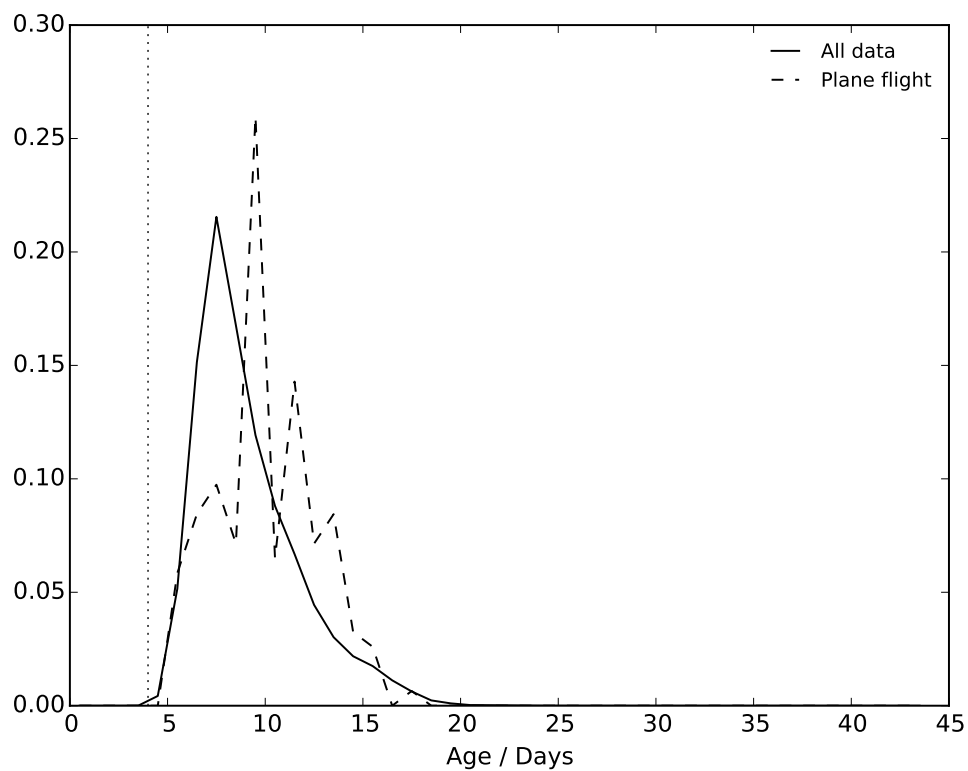
Figure B.2. Probability distribution of the physical age of CH_3I for the 3-D study domain (solid line) and as sampled by the aircraft (dashed line) between 11–15 km during CONTRAST, 18th January–28th February, 2014. The dotted line indicates $1\tau_{CH_3I}$ of 4 days.